Comparison of node-centered and cell-centered unstructured finite-volume discretizations: viscous fluxes

Boris Diskin[*]   James L. Thomas[†]   Eric J. Nielsen[‡]   Hiroaki Nishikawa[§]

Jeffery A. White[¶]

Discretization of the viscous terms in current finite-volume unstructured-grid schemes are compared using node-centered and cell-centered approaches in two dimensions. Accuracy and complexity are studied for four nominally second-order accurate schemes: a node-centered scheme and three cell-centered schemes – a node-averaging scheme and two schemes with nearest-neighbor and adaptive compact stencils for least-square face gradient reconstruction. The grids considered range from structured (regular) grids to irregular grids composed of arbitrary mixtures of triangles and quadrilaterals, including random perturbations of the grid points to bring out the worst possible behavior of the solution. Two classes of tests are considered. The first class of tests involves smooth manufactured solutions on both isotropic and highly anisotropic grids with discontinuous metrics, typical of those encountered in grid adaptation. The second class concerns solutions and grids varying strongly anisotropically over a curved body, typical of those encountered in high-Reynolds number turbulent flow simulations. Tests from the first class

[*]National Institute of Aerospace (NIA), 100 Exploration Way, Hampton, VA 23681, USA, Member AIAA bdiskin@nianet.org. Also Department of Mechanical and Aerospace Engineering, University of Virginia, Charlottesville, VA 22904, USA. Supported by NASA Fundamental Aeronautics Program, Supersonics Project, NRA Contract NNL07AA23C (PI: prof. N. K. Yamaleev)

[†]Computational Aerosciences Branch, NASA Langley Research Center, Mail Stop 128, Fellow AIAA, James.L.Thomas@nasa.gov.

[‡]Computational Aerosciences Branch, NASA Langley Research Center, Mail Stop 128, Senior Member AIAA, Eric.J.Nielsen@nasa.gov.

[§]National Institute of Aerospace (NIA), 100 Exploration Way, Hampton, VA 23681, USA, Member AIAA hiro@nianet.org

[¶]Computational Aerosciences Branch, NASA Langley Research Center, Mail Stop 128, Senior Member AIAA, Jeffery.A.White@nasa.gov.

indicate the face least-square methods, the node-averaging method without clipping, and the node-centered method demonstrate second-order convergence of discretization errors with very similar accuracies per degree of freedom. The tests of the second class are more discriminating. The node-centered scheme is always second order with an accuracy and complexity in linearization comparable to the best of the cell-centered schemes. In comparison, the cell-centered node-averaging schemes may degenerate on mixed grids, have a higher complexity in linearization, and can fail to converge to the exact solution when clipping of the node-averaged values is used. The cell-centered schemes using least-square face gradient reconstruction have more compact stencils with a complexity similar to that of the node-centered scheme. For simulations on highly anisotropic curved grids, the least-square methods have to be amended either by introducing a local mapping based on a distance function commonly available in practical schemes or modifying the scheme stencil to reflect the direction of strong coupling. The major conclusion is that accuracies of the node centered and the best cell-centered schemes are comparable at equivalent number of degrees of freedom.

I. Introduction

Both node-centered and cell-centered finite-volume discretizations are widely used for complex three-dimensional turbulent simulations in aerospace applications. The relative advantages of the two approaches have been extensively studied in the search for methods that are accurate, efficient, and robust over the broadest possible range of grid and solution parameters. The topic was discussed in a panel session at the 2007 AIAA Computational Fluid Dynamics conference, but a consensus did not emerge. One of the difficulties in assessing the two approaches is that comparative calculations were not completed in a controlled environment, i.e., computations were made with different codes and different degrees of freedom and the exact solutions were not known.

In this paper, we provide a controlled environment for comparing a subset of the discretization elements needed in turbulent simulations, namely that of the viscous discretization. In particular, we consider only Poisson's equation as a model of viscous discretization. We use the method of manufactured solution, so that the exact solution is known, and conduct theoretical and computational studies of both accuracy and efficiency for a range of grids.

The two-dimensional (2D) grids considered range from structured (regular) grids to irregular grids composed of arbitrary mixtures of triangles and quadrilaterals. Highly irregular grids are deliberately constructed through random perturbations of structured grids to bring out the worst possible behavior of the solution. Two classes of tests are considered. The first class of tests involves smooth manufactured solutions on both isotropic and highly anisotropic grids with discontinuous metrics, typical of those encountered in grid adaptation. The second class of tests

concerns solutions and grids varying strongly anisotropically over a curved body, typical of those encountered in high-Reynolds number turbulent flow simulations.

There are four main schemes considered, a node-centered (NC) scheme and three cell-centered (CC) schemes. The cell centered schemes include a node-averaging (CC-NA) scheme and two least-square face gradient reconstruction schemes differing in their stencils – a nearest-neighbor (CC-NN) stencil and an adaptive compact (CC-CS) stencil. The effect of clipping is studied for the CC-NA scheme. In its current version, the CC-CS scheme is applied only on triangular grids. For the second class of tests, an approximately mapped (AM) least-square approach is introduced to accommodate curved high-aspect-ratio grids. The mapping uses the distance function commonly available in practical codes and can be used with any scheme. Each of the schemes considered is nominally second-order accurate. The properties to be compared are computational complexity (operation count) and discretization accuracy at equivalent degrees of freedom.

II.   Grid terminology

This paper studies finite-volume discretization (FVD) schemes for viscous fluxes on grids that are loosely defined as irregular. There is no commonly accepted definition for irregular grids, so, for clarity, we specify the grid terminology used in this paper.

A grid is classified as *periodic* if it has (1) a periodic node connectivity pattern (i.e., the number of edges per node changes periodically) and (2) a periodic cell distribution (i.e., the grid is composed of periodically repeated combinations of cells). Thus, periodic grids can be analyzed by Fourier analysis. Grids that are derived from periodic grids by a smooth mapping are called *regular* grids. Regular grids include, but are not limited to, grids derived from Cartesian ones – triangular grids obtained by diagonal splitting with a periodic pattern, smoothly stretched grids, skewed grids, smooth curvilinear grids, etc. Grids that cannot be smoothly mapped to a periodic grid are called *irregular* grids. Grids with varying local topology are called *unstructured*, e.g., grids with the number of edges changing from node to node with no pattern.

The regular and irregular grids considered in this paper are derived from an underlying (possibly mapped) Cartesian grid with meshsizes h_x and h_y and the aspect ratio $A = \frac{h_x}{h_y}$; both meshsizes of the underlying grid are assumed to be small, $h_y \ll 1, h_x \ll 1$. Irregularities are introduced *locally* and do not affect grid topology and metrics outside of a few neighboring cells. A local grid perturbation is called *random* if it is independent of local perturbations introduced beyond some immediate neighborhood. For computational grids generated for the reported studies, grid irregularities are introduced in two ways (both local and random): (1) the quadrilateral cells of the underlying grid are randomly split (or not split) into triangles; (2) the grid nodes are perturbed from their original positions by random shifts; the shifts are fractions of a local meshsize.

Six grid types are considered: (I) *regular quadrilateral* (i.e., mapped Cartesian) grids; (II) *regular triangular grids* derived from the regular quadrilateral grids by the same diagonal splitting of each quadrangle; (III) *random triangular grids*, in which regular quadrangles are split by randomly chosen diagonals, each diagonal orientation occurring with probability of half; (IV) *perturbed triangular grids*, which are random triangular grids, with grid nodes perturbed from their initial positions by random shifts; (V) *perturbed quadrilateral grids*, which are quadrilateral grids with randomly perturbed grid nodes; and (VI) *perturbed mixed-element grids*, in which perturbed quadrangles are randomly split or not split by randomly chosen diagonals. Grids of types (III), (IV), and (VI) are irregular because there is no periodic connectivity pattern. Grids of types (IV)-(VI) are irregular because there is no periodic cell distribution. The representative grids are shown in Figure 1.

Our main interest is the accuracy of FVD schemes on general irregular (mostly unstructured) grids with a minimum set of constraints. In particular, we do not require any grid smoothness, neither on individual grids nor in the limit of grid refinement. The only major requirement for a sequence of refined grids is to satisfy the *consistent refinement property*. The property requires the maximum distance across the grid cells to decrease consistently with increase of the total number of grid points, *N*. In particular, the maximum distance should tend to zero as $N^{-1/2}$ in 2D computations. For three-dimensional (3D) unstructured grids, the consistent refinement property is studied in [1]. On 2D grids, the *effective meshsize*, h_e, is computed as the L_1 norm of the square root of the control volumes.

The locations of discrete solutions are called *data points*. For consistency with the 3D terminology, the 2D cell boundaries are called faces, and the term "edge" refers to a line, possibly virtual, connecting the neighboring data points. Each face is characterized by two vectors: (1) the *edge vector*, which connects the data points of the cells sharing the face and (2) the *directed-area vector*, which is normal to the face and has the amplitude equal to the face area. For each cell/face combination, the vectors are directed outward. *Local grid skewness* is measured at a face as the *skew angle* between the edge vector and the directed-area vector; small skew angles correspond to low skewness. On grids with convex cells, the maximum skewness is bounded by $90°$; on more general grids with non-convex cells, the skew angle can approach $180°$.

For most of the computational tests, the random node perturbation in each dimension is defined as $\frac{1}{4}rh$, where $r \in [-1, 1]$ is a random number and h is the local meshsize along the given dimension. With these perturbations, triangular cells in the rectangular geometry are allowed to collapse, i.e., a cell may become a zero-volume cell, albeit with a probability approaching zero. The random perturbations are introduced independently on all grids in grid refinement implying that grids of types (IV)-(VI) are grids with discontinuous metrics, e.g., ratios of neighboring cell volumes and face areas are random on all grids and do not approach unity in the limit of grid refinement.
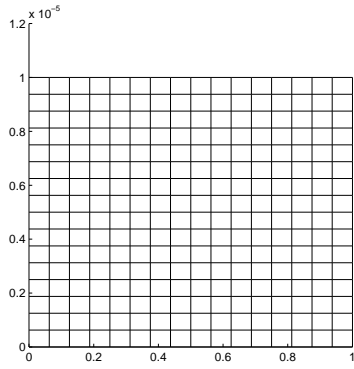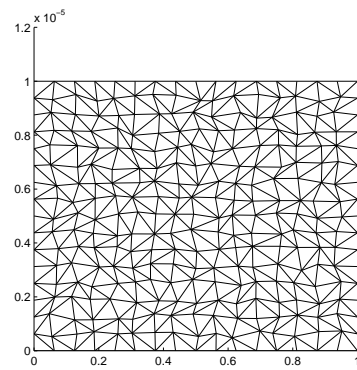
(a) Type (I): Regular quadrilateral grid
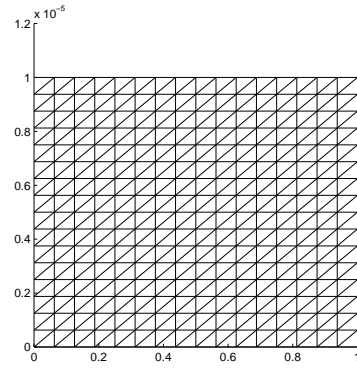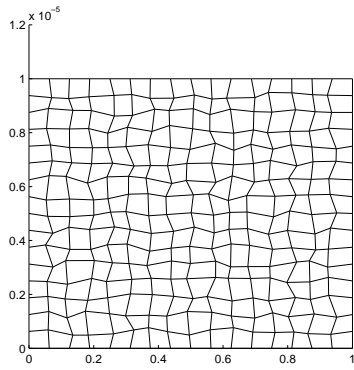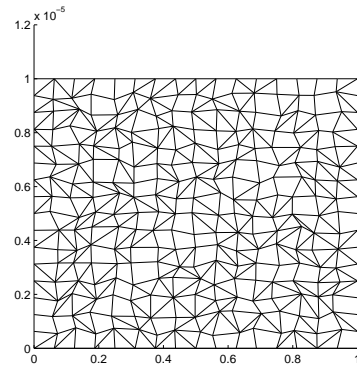

(b) Type (II): Regular triangular grid
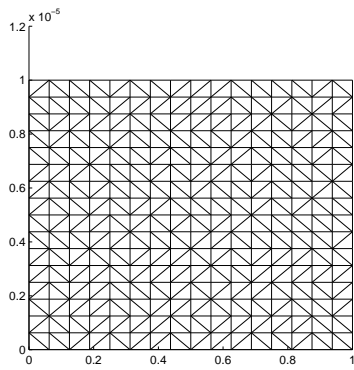
(c) Type (III): Random triangular grid

(d) Type (IV): Perturbed triangular grid

(e) Type (V): Perturbed quadrilateral grid

(f) Type (VI): Perturbed mixed grid

Figure 1. Typical regular and irregular high-aspect-ratio grids with vertical scale expanded for better visualization.

III. Finite-volume discretization schemes

The considered model problem is the Poisson equation

$$\Delta U = f, \tag{1}$$

subject to Dirichlet boundary conditions; function f is a forcing function independent of the solution. The 2D primal meshes generated for this study are composed of triangular and quadrilateral cells. The FVD schemes are derived from the integral form of a conservation law

$$\oint_\Gamma \nabla U \cdot \hat{\mathbf{n}} \, d\Gamma = \iint_\Omega f \, d\Omega, \tag{2}$$

where ∇U is the solution gradient, Ω is a control volume with boundary Γ, and $\hat{\mathbf{n}}$ is the outward unit normal vector. The general FVD approach requires partitioning the domain into a set of non-overlapping control volumes and numerically implementing equation (2) over each control volume.

Cell-centered and node-centered discretizations are considered. *Cell-centered discretizations* assume solutions are defined at the centers of the primal grid cells with the primal cells serving as the control volumes. The cell center coordinates are typically defined as the averages of the co-ordinates of the cell's vertexes. *Node-centered discretizations* assume solutions are defined at the primal mesh nodes. For node-centered schemes, control volumes are constructed around the mesh nodes by the median-dual partition: the centers of primal cells are connected with the midpoints of the surrounding faces. These non-overlapping control volumes cover the entire computational domain and compose a mesh that is dual to the primal mesh. Both cell-centered and node-centered control-volume partitions are illustrated in Figure 2.

Figure 2. Control-volume partitioning for finite-volume discretizations. Numbers $0 - 12$ and letters $A - L$ denote grid nodes and primal cell centers, respectively. The control volume for a node-centered discretization around the grid node 0 is shaded. The control volume for a cell-centered discretization around the cell center A is hashed.

A. Cell-centered FVD schemes

In cell-centered discretizations, the conservation law (2) is enforced on control volumes that are primary cells. The flux at a face is computed as the inner product of the solution gradient at the face and the directed-area vector. With refer-
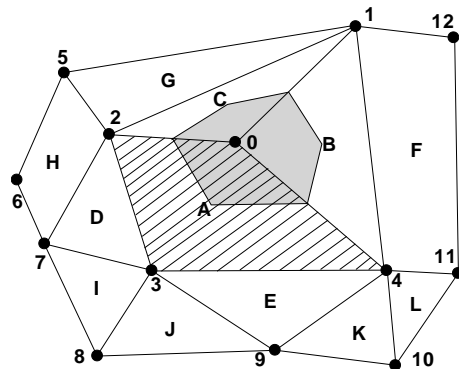
ence to Figure 2, the gradient, ∇U_{04}, at the face linking nodes 0 and 4 is found by satisfying two relations:

1. $(\nabla U_{04} \cdot \mathbf{e}_{AB}^{edge}) = \frac{U_B - U_A}{|\mathbf{r}_B^c - \mathbf{r}_A^c|}$, where $\mathbf{e}_{AB}^{edge} = \frac{\mathbf{r}_B^c - \mathbf{r}_A^c}{|\mathbf{r}_B^c - \mathbf{r}_A^c|}$ is the edge $[AB]$ unit vector; U_A and U_B are the solutions defined at the cell centers; $\mathbf{r}_A^c$ and $\mathbf{r}_B^c$ are the cell-center coordinate vectors.

2. $(\nabla U_{04} \cdot \mathbf{e}_{04}^{face}) = |\nabla U^{face}|$, where $\mathbf{e}_{04}^{face} = \frac{\mathbf{r}_4^n - \mathbf{r}_0^n}{|\mathbf{r}_4^n - \mathbf{r}_0^n|}$ is the face unit vector and $|\nabla U^{face}|$ is the solution derivative computed along the face $[0, 4]$; $\mathbf{r}_i^n$ is a coordinate vector of the node i.

The cell-centered FVD schemes considered in this paper differ only in computing $|\nabla U^{face}|$.

1. Cell-centered node-averaging FVD schemes

In the CC-NA schemes, the solution derivative along the face is computed as the divided difference between the solution values reconstructed at the nodes from the surrounding cell centers. With respect to Figure 2, the solution at the node 0 is reconstructed by averaging solutions defined at the cell centers $A, B,$ and C. The solution reconstruction proposed in [2, 3] and used in [4] is an averaging procedure that is based on a constrained optimization to satisfy some Laplacian properties. The scheme is second-order accurate and stable when the coefficients of the introduced pseudo-Laplacian operator are close to 1. It has been shown[5] that this averaging procedure is equivalent to an unweighted least-square linear fit. The gradient is resolved from the derivative along the face and the derivative along the edge connecting the cell centers across the face. For the face $[0, 4]$, the face derivative is computed using solutions reconstructed by node averaging at the nodes 0 and 4; the edge derivative is computed using solutions at cell centers A and B.

On highly stretched and deformed grids, some coefficients of the pseudo-Laplacian may become negative or larger than 2, which has a detrimental effect on stability and robustness.[6,7] Holmes and Connell[2] proposed to enforce stability by clipping the coefficients between 0 and 2. The CC-NA schemes with clipping represent a current standard in practical computational fluid dynamics (CFD) for applications involving cell-centered finite volume formulations.[8] As shown further in the paper, clipping seriously degrades the solution accuracy.

2. Cell-centered face-least-square scheme

An alternative cell-centered scheme relies on a face-based least-square method. First, an auxiliary face gradient is reconstructed within a face using a least-square procedure. The derivative along the face, $|\nabla U^{face}|$, is computed by inner product of the auxiliary gradient with the face tangent (unit) vector.
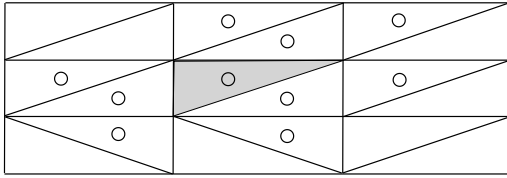
The two approaches to determine stencils for the least-square linear fit at a face are described as follows. The nearest-neighbor CC-NN six-point stencil includes the two prime cells sharing the
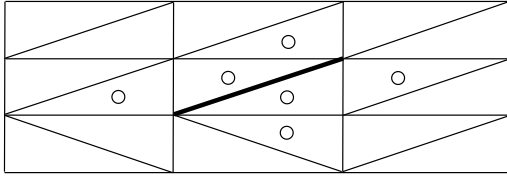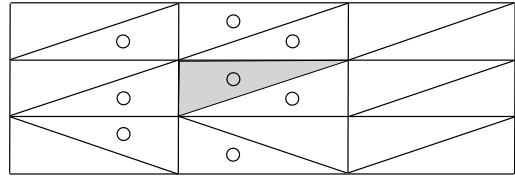
(a) Face least-square stencil with CC-NN scheme
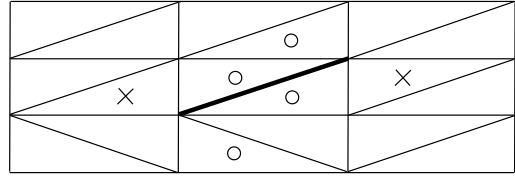
(b) Face least-square stencil with CC-CS scheme

(c) Cell Laplacian stencil with CC-NN scheme

(d) Cell Laplacian stencil with CC-CS scheme

Figure 3. Stencils on high-aspect-ratio grids of type (III). Figures are vertically expanded for better visualization.

face and their face neighbors that share one of the face nodes. In Figure 3(a), the CC-NN stencil for the highlighted face is denoted by circles.

The adaptive compact stencil (CC-CS) is important for discretizations on high-aspect-ratio grids of types (II) and (III) to represent correctly the direction of the strong coupling. It is constructed by choosing between two stencils for face least-square gradient reconstruction: a six-point stencil and a four-point stencil. In general, the four-point stencil is intended for "long" faces of high-aspect-ratio grids in local geometries resembling a layer formation.

Technically, at each face, the CC-CS method first attempts to construct a six-point stencil by combining two prime cells and four auxiliary cells; each auxiliary cell is associated with a prime cell and a face node. The method chooses the auxiliary cell that (1) shares the face node, (2) is located on the opposite side of the face from the associated prime cell center, (3) is not already in the stencil, and (4) has the shortest distance to the center of the associated prime cell. The six-point stencil for the highlighted diagonal face is denoted by the union of circles and crosses in Figure 3(b). In the process of construction, each prime cell identifies the closest associated

auxiliary cell, which is called its mirror image. The four-point stencil is defined by prime cells and their mirror images and shown as circles in Figure 3(b).

The CC-CS method selects the four-point stencil, if either the six-point stencil cannot be formed following the rules (1)-(4), which may happen next to the boundaries or in curved geometries, or the four-point stencil represents an ideal pair-wise construction. The four-point pair-wise construction is considered ideal, if the data points within the pairs of prime-cell/mirror-image are very close (closer than a predefined distance threshold) and have a low skewing (the angle between the vector connecting the prime cell center with its mirror image and the face directed area vector is smaller than a predefined skew threshold). For computations on high-aspect-ratio grids, the distance threshold has been chosen as three times the smaller mesh size of the background grid and the skew threshold has been set to $\sin^{-1}(0.1)$. The four-point stencil in Figure 3(b) is considered ideal.

Figures 3(c) and 3(d) compare CC-NN and CC-CS FVD stencils on the shaded cell. CC-CS FVD scheme uses four-point stencils for diagonal and horizontal faces and a six-point stencil for the vertical face. The CC-CS stencil is more compact than the CC-NN stencil and provides a three-point vertical structure centered at the shaded cell center that better reflects the grid anisotropy direction.

Remark. It is known that on high-aspect-ratio curved grids, unweighted least-square methods have difficulties with reconstructing accurate gradients within a cell.[9–11] Inverse-distance weighting has been shown to improve gradient accuracy. For face-centered least-square reconstruction, the usual weightings, with distances measured from the face center, do not improve gradient accuracy because all points involved in least-square stencils are typically at comparable distances from the face center. A modified weighting, which is based on (minimal) distances from the two cell centers across the face, with an extended stencil (the stencil that is used in CC-NA scheme) improves gradient accuracy on high-aspect-ratio curved grids derived by an advanced layer method. The weighting effectively reduces the extended stencil to the four-point stencil of the CC-CS scheme. However, the method led to unstable formulations on general irregular grids and was not pursued further.

B.   Node-centered FVD scheme

The second-order accurate node-centered FVD scheme illustrated by Figure 4 represents a standard CFD approach to node-centered viscous discretizations. The scheme approximates the integral flux through the dual faces adjacent to the edge $[P_0, P_4]$ as

$$\int_{ABC} \nabla U \cdot \hat{\mathbf{n}} \, d\Gamma = \nabla U^R \cdot \mathbf{n_R} + \nabla U^L \cdot \mathbf{n_L}. \tag{3}$$

The gradient is reconstructed separately at each dual face as follows.

For the triangular element contribution, the gradient is determined from a Green-Gauss evaluation at the primal-grid element,

$$\nabla U^L = \overline{\nabla U}_{014}. \tag{4}$$

The gradient overbar denotes a gradient evaluated by the Green-Gauss formula on the primal cell identified by the point subscripts. With fully-triangular elements, the formulation is equivalent to a Galerkin finite element scheme with a linear basis function.[6,12] Analysis in Appendix A shows that on triangular grids of types (II) and (III) in rectangular geometries, the formulation recovers the five-point Laplacian stencil of the type (I) grids, independent of aspect ratio.
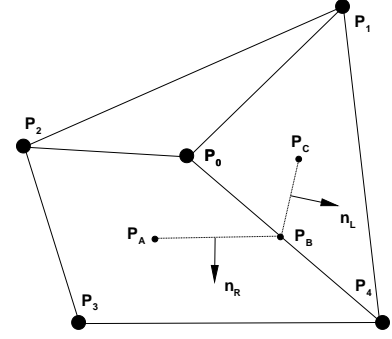

Figure 4. Illustration of gradient reconstruction for viscous terms on mixed grids with median-dual partition.

For the quadrilateral element contribution, the gradient is evaluated as

$$\nabla U^R = \overline{\nabla U}_{0234} + \left[|\nabla U^E| - \overline{\nabla U}_{0234} \cdot \mathbf{e}_{04} \right] \mathbf{e}_{04}, \tag{5}$$

where

$$|\nabla U^E| = \frac{U_4 - U_0}{|\mathbf{r}_4^p - \mathbf{r}_0^p|} \tag{6}$$

is the edge gradient computed at the median P_B of the edge $[P_0, P_4]$, U_i and $\mathbf{r}_i^p$ are the solution and the coordinate vector of the node P_i, and

$$\mathbf{e}_{04} = \frac{\mathbf{r}_4^p - \mathbf{r}_0^p}{|\mathbf{r}_4^p - \mathbf{r}_0^p|} \tag{7}$$

is the unit vector aligned with the edge $[P_0, P_4]$. Note that for grids with dual faces perpendicular to the edges, the edge-gradient, $|\nabla U^E|$, is the only contributor. This approach to the gradient reconstruction is used to decrease the scheme susceptibility to odd-even decoupling.[13,14] It has been shown[1,15] that the scheme possesses second-order accuracy for viscous fluxes on general isotropic mixed-element grids.

IV.   Complexity of discretization stencils

The size of the stencil for the viscous discretization is examined for 2D and 3D cell-centered and node-centered FVD schemes. Estimates are made for Cartesian meshes split into triangular and tetrahedral elements and neglecting any boundary effects. Estimates are compared to a numerical

calculation on an actual 3D turbulent viscous grid that includes boundary effects.

In two dimensions, two splittings of the Cartesian grid are considered. The first splits each quadrilateral cell with a diagonal oriented in the same direction. The second splits the cells with diagonals of face-adjacent quadrilaterals oriented in the opposite direction. The second splitting is slightly more analogous to the 3D splitting. In three dimensions, half of the grid nodes have 18 incident edges (32 incident tetrahedra) and half have 6 incident edges (8 incident tetrahedra). Each of the tetrahedra interior to an originally-hexahedral cell is defined by four nodes, each with 18 incident edges. Each of the four surrounding tetrahedra within an originally-hexahedral cell is defined by three nodes with 18 incident edges and 1 node with 6 incident edges. For reference, Table 1 shows the average and maximum number of edges, n_{edge}, connecting to a grid node. The average number of connecting edges sets the stencil size for the node-centered scheme as $s = n_{edge} + 1$. The number of connecting edges is also an important factor in the CC-NA schemes because the gradients in the control volumes faces are computed from cell-centered data averaged to the grid nodes.[8]

Dimension	n_{edge} (Average)	n_{edge} (Maximum)
2D	6	8
3D	12	18

Table 1. Edges connecting to a grid node in the split Cartesian grids.

Node-centered	CC-NA	CC-NN
7	13/16	10/9

Table 2. Size of the viscous stencil for 2D discretizations with triangular elements.

	Node-centered	CC-NA	CC-NN
Estimate	13	79	15
Numerical	14	69	15

Table 3. Average size of the viscous stencil for 3D discretizations with tetrahedral elements.

Table 2 shows stencil-size estimates for 2D triangular grids. There is a slight difference in the estimates from the two splittings (entries separated by slashes in the table), depending on the diagonalization pattern. The CC-NA stencil is the largest. Table 3 shows stencil-size estimates for 3D tetrahedral grids. The CC-NA stencil is again the largest. The CC-NN stencil is only slightly larger than the stencil of the node-centered discretization, in both estimation and computation. The

complexity of the CC-CS stencil is even smaller.

Because the computational stencil of the CC-NA scheme is very large, direct relaxation of the full linearization operator is prohibitively expensive in terms of CPU time and memory resources. Defect-correction iterations are widely used as a practical solution method. A common driver used for defect-correction iterations is an edge-based thin-shear-layer (TSL) FVD scheme. Although the TSL schemes are not accurate on general grids (accuracy of TSL FVD schemes is zeroth order on general grids), the defect-correction method is efficient on grids with low skewing. It has been shown[16] that for high grid skewing, unavoidable in highly anisotropic triangular/tetrahedral grids used for high Reynolds number simulations, efficiency and stability of defect-correction methods with TSL drivers degrade leading to explicit stability (CFL) limitations.

V. Analysis methods

A. Method of manufactured solution

Accuracy of FVD schemes is analyzed for known exact or manufactured solutions. The forcing function and boundary values are found by substituting this solution into the Poisson equation with Dirichlet boundary conditions. The discrete forcing function is defined at the data points.

1. Discretization error

The main accuracy measure is the *discretization error*, E_d, which is defined as the difference between the exact discrete solution, U^h, of the discretized equations (2) and the exact continuous solution, U, to the differential equation (1)

$$E_d = U - U^h; \tag{8}$$

U is sampled at data points.

2. Truncation error

Another accuracy measure commonly used in computations is *truncation error*. Truncation error, E_t, characterizes the accuracy of approximating the differential equation (1). For finite differences, it is defined as the residual obtained after substituting the exact solution U into the discretized differential equations.[17] For FVD schemes, the traditional truncation error is usually defined from the time-dependent standpoint.[18,19] In the steady-state limit, it is defined (e.g., in [20]) as the

residual computed after substituting U into the normalized discrete equations (2),

$$E_t = \frac{1}{|\Omega|} \left[-\iint_\Omega f^h \, d\Omega + \oint_\Gamma (\nabla U \cdot \hat{\mathbf{n}}) \, d\Gamma \right], \tag{9}$$

where $|\Omega|$ is the measure of the control volume,

$$|\Omega| = \iint_\Omega d\Omega, \tag{10}$$

f^h is an approximation of the forcing function f on Ω, and the integrals are computed according to some quadrature formulas. Note that convergence of truncation errors is expected to show the order property only on regular grids; on irregular grids, it has been long known that the design-order discretization-error convergence can be achieved even when truncation errors exhibit a lower-order convergence or, in some cases, do not converge at all.[20–22]

3. Accuracy of gradient reconstruction

Yet another important accuracy measure is the accuracy of gradient approximation at a control-volume face. For second-order convergence of discretization errors, the gradient is usually required to be approximated with at least first order. For each face, accuracy of the gradient is evaluated by comparing the reconstructed gradient, ∇_r, with the exact gradient, ∇_{exact}, computed at the face center. The accuracy of gradient reconstruction is measured as the relative gradient error:

$$E_{\text{rel}} = \frac{\|\epsilon\|}{\|G\|}, \tag{11}$$

where functions ϵ and G define face-wise amplitudes of the gradient error and the exact gradient, respectively,

$$\epsilon = |\nabla_r U^h - \nabla_{\text{exact}} U|, \qquad \text{and} \qquad G = |\nabla_{\text{exact}} U|; \tag{12}$$

U and U^h are a differentiable manufactured solution and its discrete representation (usually injection) on a given grid, respectively; $\|\cdot\|$ is a norm of interest computed over the entire computational domain.

VI. Isotropic irregular grids

A. Grid refinement

A sequence of consistently refined grids of type (IV) is generated on the unit square $[0, 1] \times [0, 1]$. Irregularities are introduced at each grid independently, so the grid metrics remain discontinuous on all the grids. The ratio of areas of neighboring faces can be as large as $3\sqrt{2}$; because a control volume can be arbitrary small, the ratio of the neighboring volumes can be arbitrary high. Isotropic grids randomly generated for this study have 0.01% of cell volumes smaller than $\frac{1}{10}\frac{1}{N^2}$; the total number of grids nodes is $(N + 1)^2$; about 0.006% of interior faces have skew angles larger than $70°$.

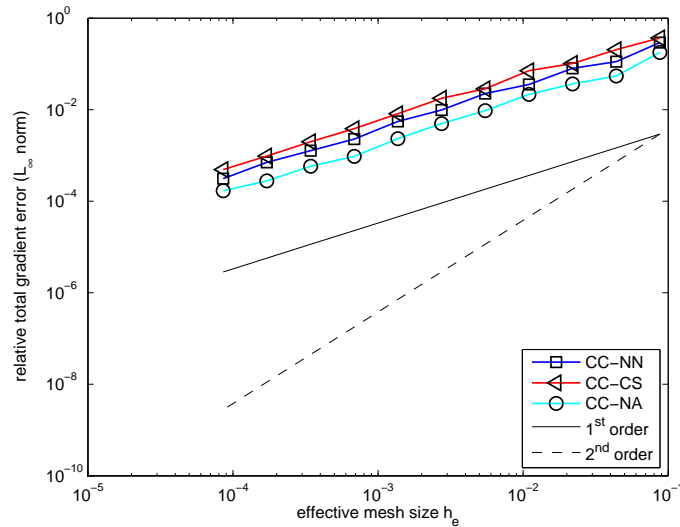## B. Gradient reconstruction accuracy

Figure 5. Accuracy of gradient reconstruction on isotropic irregular grids

The accuracy of gradient reconstruction for isotropic irregular grids is first order for all methods,[23] which is sufficient for second-order discretization accuracy. As an example, the gradient reconstruction tests are performed for the manufactured solution $U = \sin(\pi x + 2\pi y)$. Figure 5 shows convergence of the L_∞ norms of relative gradient errors computed for cell-centered schemes on a sequence of refined grids of type (IV). All methods provide first-order gradient approximations and very similar relative errors.

C. Convergence of truncation and discretization error

The numerical tests evaluating convergence of truncation and discretization errors are performed with Dirichlet boundary conditions specified from the manufactured solution $U = \sin(\pi x + 2\pi y)$. For cell-centered formulations, the solution is specified on all cells linked to the boundary. Figure 6 shows convergence of the L_1 norms of truncation and discretization errors for the node-centered and two cell-centered formulations on grids of type (IV). As predicted in [1, 15], truncation errors do not converge on irregular grids in any norm. Discretization errors converge with second order for all formulations considered. The discretization errors of the cell-centered and node-centered FVD schemes are almost over-plotted, indicating a similar accuracy per degree of freedom, which implies better accuracy for the cell-centered FVD schemes on the same grids, as expected.
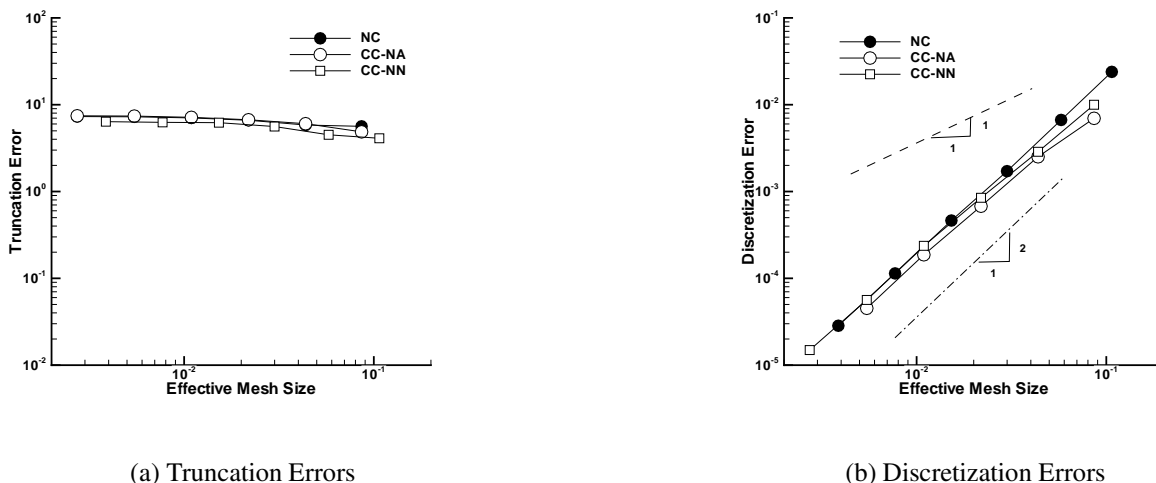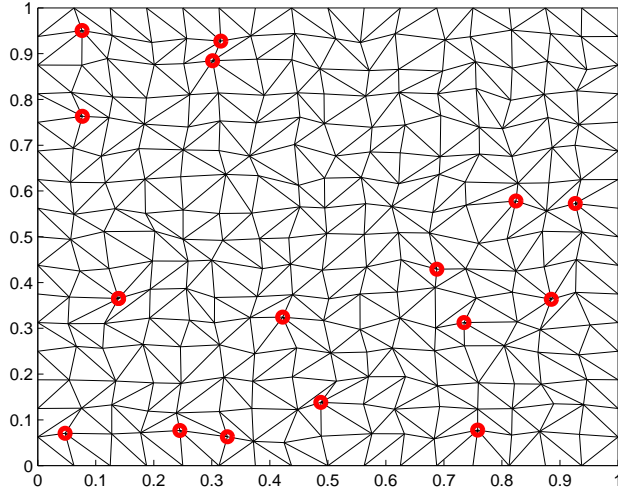

(a) Truncation Errors   (b) Discretization Errors

Figure 6. Convergence of L_1-norms of truncation and discretization errors on random triangular grids of type (IV).

D. Effects of clipping

The tests reported in this section are performed for the CC-NA schemes and demonstrate detrimental effects of clipping on accuracy of gradient approximation and on the discretization accuracy. The accuracy is evaluated for the manufactured solution $U = \sin(2\pi y)$. Dirichlet boundary conditions over-specified from the manufactured solution are imposed at all control volumes connecting to the boundary. Considered irregular grids of type (IV) are derived from underlying isotropic (unit aspect ratio) Cartesian grids covering the unit square. Figure 7(a) shows an example of an isotropic random triangular grid of type (IV) with 17^2 nodes; nodes where clipping occurs in reconstruction are circled; about 7% of the interior nodes are clipped.

It has been demonstrated in [16] that the face gradients computed by the CC-NA scheme with

(a) Random triangular grid with 17^2 nodes. Clipped nodes are circled.
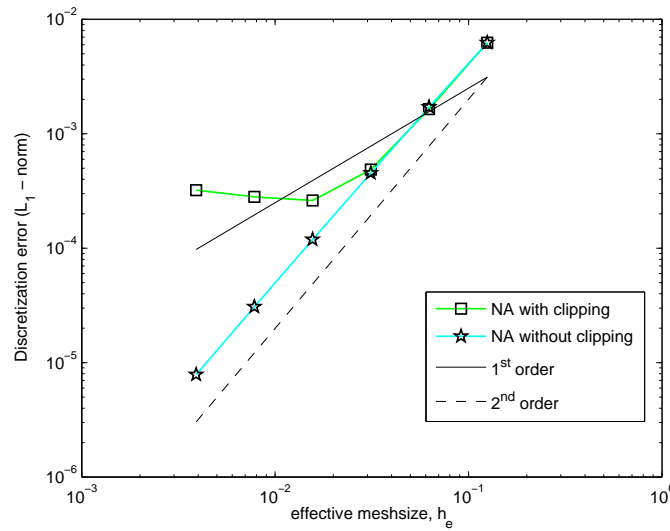
(b) Discretization errors

Figure 7. Accuracy of CC-NA schemes on isotropic irregular triangular grids of type (IV)

clipping do not approximate the exact gradients on grids of type (IV). The normal and tangential components of the computational gradients have been evaluated within interior faces and compared with the exact-gradient components at the face center. The maximum norms of the deviations between the computational and the exact-gradient components have not converged in grid refinement. The CC-NA scheme without clipping provides a first-order accurate gradient approximation. Fig-

ure 7(b) exhibits convergence of the L_1 norms of discretization errors. The no-clipping CC-NA scheme demonstrates second-order convergence; convergence of the CC-NA scheme with clipping appears as second order on the coarse grids, but then degrades to zeroth order. Although not shown, the L_∞ norms of discretization errors converge with the same orders as the corresponding L_1 norms.

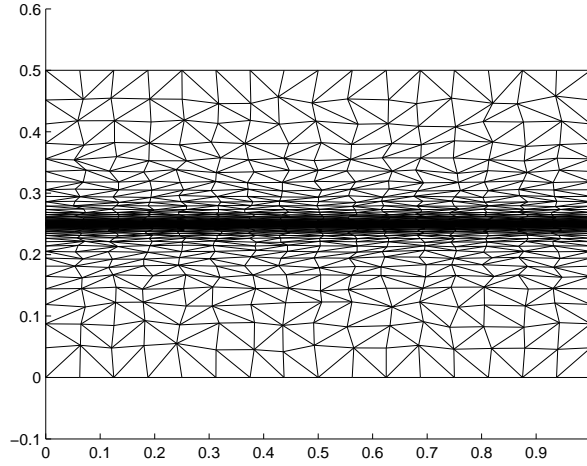## VII. Anisotropic irregular grids

Figure 8. Random triangular stretched grid with 17×65 nodes

In this section, we study FVD schemes on irregular stretched grids generated on rectangular domains. Figure 8 shows an example grid with the maximal aspect ratio $A = 1000$. A sequence of consistently refined stretched grids is generated on the rectangle $(x, y) \in [0, 1] \times [0, 0.5]$ in the following 3 steps.

1. A background regular rectangular grid with $(N_x + 1) \times (N_y + 1)$ nodes and the horizontal mesh spacing $h_x = \frac{1}{N_x}$ is stretched toward the horizontal line $y = 0.25$. The y-coordinates of the horizontal grid lines in the top half of the domain are defined as

$$y_{\frac{N_y}{2}+1} = 0.25; \qquad y_j = y_{j-1} + \hat{h}_y \beta^{j-\left(\frac{N_y}{2}+1\right)}, \qquad j = \frac{N_y}{2} + 2, \ldots, N_y, N_y + 1. \quad (13)$$

Here $\hat{h}_y = \frac{h_x}{A}$ is the minimal mesh spacing between the vertical lines; $A = 1000$ is a fixed maximal aspect ratio; β is a stretching factor, which is found from the condition $y_{N_y+1} = 1$. The stretching in the bottom half of the domain is defined analogously.

2. Irregularities are introduced by random shifts of interior nodes in the vertical and horizontal directions. The vertical shift is defined as $\Delta y_j = \frac{3}{16}\rho \min(h_y^{j-1}, h_y^j)$, where ρ is a random number between -1 and 1, and h_y^{j-1} and h_y^j are vertical mesh spacings on the background stretched mesh around the grid node. The horizontal shift is introduced analogously, $\Delta x_i = \frac{3}{16}\rho h_x$. With this random node perturbations, all perturbed quadrilateral cells are convex.

3. Each perturbed quadrilateral is randomly triangulated with one of the two diagonal choices; each choice occurs with a probability of one half.

A recent study[23] assessed accuracy of gradient approximation on various irregular grids with high aspect ratio $A = \frac{h_y}{h_x} \gg 1$. The study indicates that for rectangular geometries and functions predominantly varying in the direction of small mesh spacing (y-direction), gradient reconstruction is accurate. For manufactured solutions significantly varying in the direction of larger mesh spacing (x-direction), the face-gradient reconstruction may produce extremely large $O(Ah_x)$ relative errors affecting the accuracy of the y-directional gradient component. Figure 9 shows examples of first-order accurate gradient approximations that exhibit large relative errors on high-aspect-ratio grids of type (III).
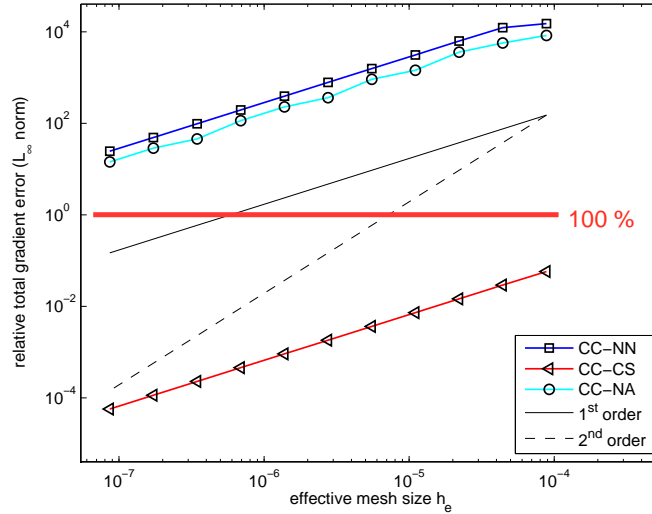
Figure 9. Large relative errors in approximation of face gradients are observed for the manufactured solution $U = \sin(\pi x + 2\pi y)$ **on anisotropic grids of type (III) with** $A = 10^6$.

A summary of the previous results[23] for grids of types (I)-(VI) (supplemented by the results for the CC-CS scheme) is presented in Table 4. All considered gradient reconstruction methods may generate large relative errors on irregular grids of types (IV)-(VI) with perturbed nodes. The CC-NA and CC-NN methods may also have large relative errors on grids of types (II) and (III); the NC method using the Green-Gauss approach and the CC-CS method always provide accurate

gradients on these grids.

Table 4. Relative error of gradient reconstruction

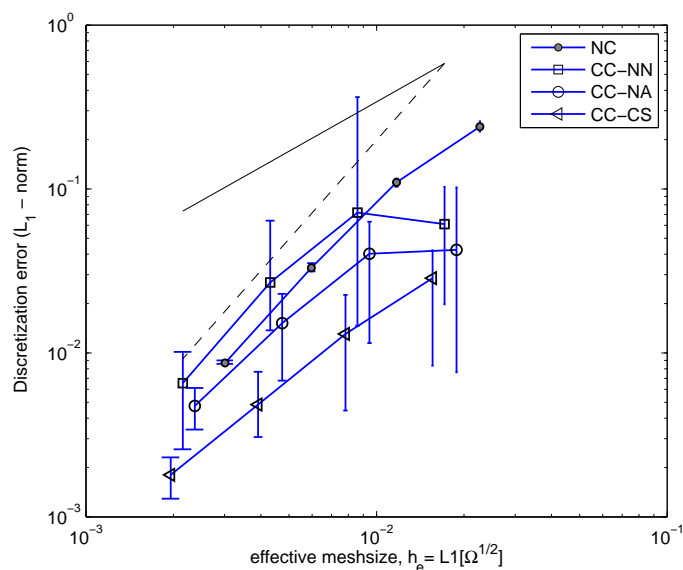| Grids	(I)	(II)	(III)	(IV) –(VI)
NC	$O(h_x^2)$	$O(h_x^2)$	$O(h_x)$	$O(Ah_x)$
CC-NA	$O(h_x^2)$	$O(Ah_x^2)$	$O(Ah_x)$	$O(Ah_x)$
CC-NN	$O(h_x^2)$	$O(Ah_x^2)$	$O(Ah_x)$	$O(Ah_x)$
CC-CS	$O(h_x^2)$	$O(h_x^2)$	$O(h_x)$	$O(Ah_x)$

Figure 10. Convergence of discretization errors for solution $U = \sin(\pi x + 2\pi y)$ **on stretched grids of type (IV)**

A poor gradient reconstruction accuracy, however, does not necessarily imply large discretization error. Mavriplis[9] reported (second-order) accurate node-centered solutions even on grids with large gradient reconstruction errors. Here, we observe similar results for cell-centered and node-centered formulations.

Convergence of the L_1 norms of discretization errors for the manufactured solution $U = \sin(\pi x + 2\pi y)$ on a sequence of consistently refined stretched grids of type (IV) (see Figure 8) is shown in Figure 10. All tests have been performed stochastically, i.e., several grids (ten) with different irregularities patterns have been independently generated on each scale (same number of nodes). The plot symbols indicate the mean errors and bars indicate the maximum and minimum errors observed on each scale. The effective meshsize is practically the same for all cell-centered schemes at a given scale, but, for visualization purposes, plots of the CC-NA and CC-CS schemes

are shifted to the right and the left, respectively, of the CC-NN scheme.

All discretization errors are relatively small and converge with second order. The error of the CC-CS scheme is the smallest. The variation of discretization errors at a given scale is largest with the CC-NN scheme. The NC scheme is remarkably insensitive to grid irregularities. This property is probably explained by smaller variations (less significant irregularity) of control volumes observed for the node-centered formulation on the considered grids; the ratio of neighboring control volumes is always bounded and typically close to unity. As mentioned above, in cell-centered formulations on grids of types (IV)-(VI), the ratio of neighboring control volumes can be very high. Note that for cell-centered formulations on grids of types (I)-(III), the ratio of the neighboring control volumes is also close to unity; thus, error variations on such grids are expected to be smaller. Error variations for all schemes are getting smaller on finer grids. Overall, the levels of discretization errors obtained with the node-centered and cell-centered schemes are similar at comparable degrees of freedom.

VIII.   Grids with curvature and high aspect ratio

In this section, we discuss accuracy of FVD schemes on grids with large deformations induced by a combination of curvature and high aspect ratio. The grid nodes are generated from a cylindrical mapping where (r, θ) denote polar coordinates with spacings of h_r and h_θ, respectively; the innermost radius is $r = R$. The grid aspect ratio is defined as the ratio of mesh sizes in the circumferential and the radial directions, $A = \frac{Rh_\theta}{h_r}$. The mesh deformation is characterized by the parameter Γ:

$$\Gamma = \frac{R\left(1 - \cos(h_\theta)\right)}{h_r} \approx \frac{Rh_\theta^2}{2h_r} = A\frac{h_\theta}{2}. \tag{14}$$

The following assumptions are made about the range of parameters: $R \approx 1$, $A \gg 1$, and $\Gamma h_r \ll 1$, which implies that both h_r and h_θ are small. For a given value of A, the parameter Γ may vary: $\Gamma \gg 1$ corresponds to meshes with large curvature-induced deformation; $\Gamma \ll 1$ indicates meshes that are locally (almost) Cartesian. In a mesh refinement that keeps A fixed, $\Gamma = O(Ah_\theta)$ asymptotes to zero. This property implies that on fine enough grids with fixed curvature and aspect ratio the discretization error convergence is expected to be the same as on similar grids generated on rectangular domains with no curvature.

We are focusing on convergence of discretization errors on high-Γ grids with large curvature-induced deformations, following a previous study[23] focused on gradient accuracy. Considered manufactured solutions predominantly vary in the radial direction of small mesh spacing.

Four types of 2D grids are considered for the cylindrical geometry: (I) *regular quadrilateral*

grids; (II) *regular triangular grids* derived from the regular quadrilateral grids by the same diagonal splitting of each quadrangle; (III) *random triangular grids*, in which regular quadrangles are split by randomly chosen diagonals, each diagonal orientation occurring with probability of half; (VI) *mixed grids*, in which regular quadrangles are randomly split or not split by randomly chosen diagonals; about half of quadrangles are split. In distinction from grids of type (VI) introduced in the previous sections, random node perturbation is not applied to high-Γ cylindrical grids because even small perturbations in the circumferential direction may lead to non-physical control volumes. Representative stretched grids of types (III) and (VI) are shown in Figures 11.
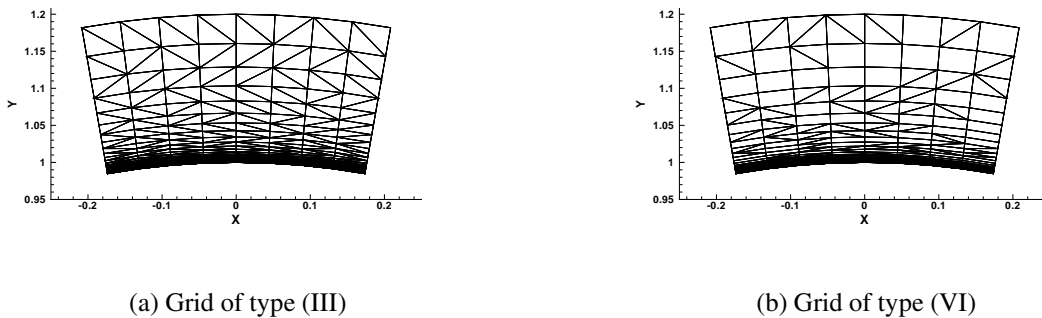

(a) Grid of type (III)   (b) Grid of type (VI)

Figure 11. Representative 9×33 stretched high-Γ grids

A.   Accuracy of gradient approximation

Previous observations and analysis[9–11] confirmed that the unweighted-least-square gradient approximation is zeroth order accurate on deformed grids with high Γ. To improve the accuracy of gradient approximation, a least-square minimization in a mapped domain is proposed. Two mapped least-square methods are considered: an exact mapping (EM) method that uses the polar coordinates directly and a more general approximate mapping (AM) method that is based on the distance function, defined as the distance to the nearest boundary, normally available in practical schemes. Applicability of the EM method is limited to model problems with analytical boundary shape.

The more general AM method approximates the EM method by applying the least-square min-

imization in a locally constructed coordinate system

$$f^r \equiv f_0 + \kappa\xi' + \lambda\eta'. \tag{15}$$

The local coordinates, (ξ', η'), are constructed using the distance function, which provides information on the closest boundary point. First the distance function is reconstructed at the face center. The coordinate vectors at the face center are defined as a unit η'-directional vector pointing in the direction opposite to the closest boundary point and its orthonormal ξ'-directional vector. The η'-coordinate is taken as the distance from the boundary and the ξ'-coordinate is the projection of the vector connecting the stencil point with the face center onto the ξ'-direction. For the cylindrical geometry, the distance function is the shifted radial function, $r - R$.

The gradient approximation accuracy for high-Γ grids of types (I)-(III) from the previous study[23] supplemented with the CC-CS and CC-NA-AM results is summarized in Table 5. Convergence of the maximum gradient errors over all faces is tabulated. Note that large $O(Ah_\theta)$ relative errors for the CC-NA scheme occur on high-Γ grids of type (III) only at the radial faces in the gradient component tangential to the face; the errors at other faces and in the gradient component normal to the radial face are small. The large relative errors for the CC-CS scheme occur for extremely large $\Gamma \gg 10^5$ at the circumferential and diagonal faces. The least-square gradient itself is accurate at these faces; the error is caused by inclusion of the edge gradient in reconstruction.

Table 5. High-Γ grids: relative errors of gradient reconstruction

	(I)	(II)	(III)
NC	$O(h_\theta^2)$	$O(h_\theta)$	$O(h_\theta)$
CC-NN	$O(h_\theta^2)$	$O(1)$	$O(1)$
CC-NN-EM	$O(h_r^2)$	$O(h_r^2)$	$O(h_r^2)$
CC-NN-AM	$O(h_\theta^2)$	$O(h_\theta^2)$	$O(h_\theta^2)$
CC-CS	$O(h_\theta^2)$	$O(Ah_\theta)$	$O(Ah_\theta)$
CC-NA	$O(h_\theta^2)$	$O(h_\theta^2)$	$O(Ah_\theta)$
CC-NA-AM	$O(h_\theta^2)$	$O(h_\theta^2)$	$O(h_\theta^2)$

B. Discretization error convergence

Discretization errors of cell-centered schemes are compared with the errors of the node-centered scheme on refined stretched high-Γ grids of types (III) and (VI). The tests are performed for the manufactured solution $U = \sin(5\pi r)$. The computational grids (see Figure 11) are derived from background regular cylindrical grids with radial extent of $1 \le r \le 1.2$ and angular extent of $20°$.

The background grids have four times more nodes in the radial direction than in the circumferential direction. The grid-refinement study is performed on grids stretched in the radial direction with a fixed maximal aspect ratio $A \approx 1000$. The maximal value of parameter Γ changes approximately from 24 to 3. The stretching ratio is changing as $\beta = 1.25, 1.11, 1.06$, and 1.03.
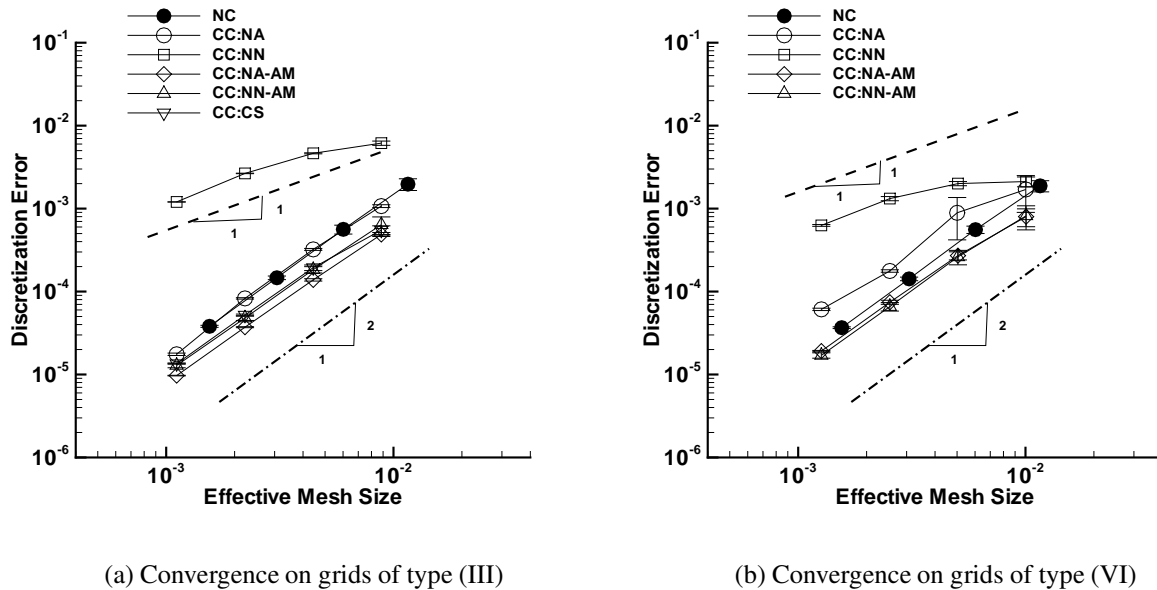

(a) Convergence on grids of type (III)

(b) Convergence on grids of type (VI)

Figure 12. Convergence of the L_1-norms of the discretization errors on high-Γ grids

Convergence of the L_1-norms of the discretization errors on grids of type (III) is shown in Figure 12(a). All tests have been performed stochastically. The plot symbols again indicate the mean errors and bars indicate the maximum and minimum errors observed on each scale. As expected, error variations observed on grids of the same scale due to grid irregularities are small for all schemes and decreasing for smaller scales (larger grids). The errors of the NC, CC-NA, CC-CS, CC-NN-AM, and CC-NA-AM solutions converge with second order and are almost over-plotted on fine grids indicating the same accuracy per degree of freedom. The errors of the CC-NN scheme are significantly higher and converge with first order.

Convergence of the L_1-norms of the discretization errors on grids of type (VI) is shown in Figure 12(b). The effective meshsizes of cell-centered and node-centered formulations are much closer on mixed grids than on triangular grids. The CC-CS scheme is omitted because its current version has been derived only for triangular cells. It is expected that a mixed-element version can be derived, but it is not currently available. Note also that the CC-NA scheme may lose stability on high-Γ mixed element grids. On these grids, there are topologies where the node solution is averaged from four neighboring cells. The four cell centers involved in such averaging may be located on a straight line, thus leading to degeneration. In these (rare) instances, large negative

contributions appear on the main diagonals of the full linearization matrix. The scheme may still be solved and even provide a reasonable accuracy. The approximately mapped version of the node averaging scheme, CC-NA-AM, is always stable.

IX. Conclusions

Node-centered (NC) and cell-centered schemes have been compared for finite-volume discretization of Poisson's equation as a model of the viscous flow terms. Among the considered schemes, the node-centered scheme has the lowest complexity, i.e., involves the least number of neighbors. The cell-centered schemes using least-square face gradient reconstruction have complexity comparable to that of the node-centered scheme. Complexity of the cell-centered node-averaging (CC-NA) scheme is the highest.

The accuracy comparisons have been made for two classes of tests: the first class is representative of adaptive-grid simulations and involves irregular grids with discontinuous metrics; the second class is representative of high-Reynolds number turbulent flow simulations over a curved body. All tests have been performed for smooth manufactured solutions.

For the tests of the first class performed in rectangular geometries on consistently refined irregular grids, all schemes demonstrated similar qualities:

(1) The discretization errors converge with second order and quantitatively are similar for all the tested schemes on grids with the same number of degrees of freedom.

(2) Gradient reconstruction may produce $O(Ah_x)$ large relative errors on grids of types (IV)-(VI); here A is the grid aspect ratio and h_x is the larger mesh spacing.

(3) Truncation errors do not converge, as expected.

The CC-NA scheme with clipping can fail to approximate gradients and/or to converge to the exact solution. Note, however, that the clipping is introduced mainly for stability of the inviscid solution and can be eliminated for the viscous terms.

The tests of the second class have been performed on consistently refined stretched grids generated around a curved body, typical of those generated by the method of advancing layers. The range of grid parameters has been chosen to enforce significant curvature-induced grid deformations, characterized by parameter Γ. These high-Γ tests proved to be more discriminating:

(1) The discretization errors are small and converge with second order for the NC scheme, for the cell-centered least-square schemes with a compact stencil (CC-CS) and for approximate mapping schemes (CC-NN-AM and CC-NA-AM). The discretization errors for the CC-NA scheme also converge with second order, but the scheme may lose stability on mixed

grids. The cell-centered nearest-neighbor scheme without mapping (CC-NN) shows first-order convergence and the highest level of discretization errors.

(2) Accurate gradient reconstruction is provided by the NC scheme and the approximate mapping schemes, CC-NN-AM and CC-NA-AM, on all grids. On high-Γ grids of types (II) and (III), the CC-NN scheme generates $O(1)$ errors in gradient reconstruction. The cell-centered CC-NA and CC-CS schemes may produce large relative gradient errors proportional to the product of the grid aspect ratio and the larger mesh spacing.

The major conclusion is that accuracies of the node centered and the best cell-centered schemes are comparable at equivalent number of degrees of freedom.

A. Node-centered discretization on grids of types (II) and (III) in rectangular geometries

In this section, we show that the node-centered (Galerkin) discretization of the Laplacian reduces to a common finite-difference formula for triangular grids for rectangular geometries of arbitrary aspect ratio. Consider a set $\{T_j\}$ of triangles/tetrahedra that share a node j. With solution values stored at nodes, the Green-Gauss gradient within each cell is given by

$$\overline{\nabla U}_T = \frac{1}{D\Omega_T} \sum_{i \in \{i_T\}} U_i \mathbf{n}_i, \tag{16}$$

where $D = 2$ for triangles, $D = 3$ for tetrahedra, Ω_T is the volume of the cell T, $\{i_T\}$ is a set of nodes of the cell T, and $\mathbf{n}_i$ is the scaled inward normal vector of the face opposite to the node i whose magnitude is equal to the face area. Then, applying the node-centered discretization as in (3) (or equivalently the standard Galerkin discretization), we obtain a discretization at j,

$$\int_{\Omega_j} \Delta U \, d\Omega_j = \int_{\Gamma_j} \nabla U \cdot \hat{\mathbf{n}} \, d\Gamma_j = - \sum_{T \in \{T_j\}} \frac{1}{D^2 \Omega_T} \sum_{i \in \{i_T\}} U_i \left(\mathbf{n}_i \cdot \mathbf{n}_j^T \right), \tag{17}$$

where Ω_j and Γ_j are respectively the dual control volume around j and its boundary, and $\mathbf{n}_j^T$ is the scaled inward normal vector opposite to the node j in the cell T. For our purpose, it is particularly convenient to separate the right-hand side of (17) into two terms:

$$\int_{\Omega_j} \Delta U \, d\Omega_j = -\frac{1}{D^2} \sum_{T \in \{T_j\}} \left(\frac{\mathbf{n}_j^T \cdot \mathbf{n}_j^T}{\Omega_T} \right) U_j - \frac{1}{D^2} \sum_{T \in \{T_j\}} \sum_{i \in \{i_T\}, i \neq j} \left(\frac{\mathbf{n}_i \cdot \mathbf{n}_j^T}{\Omega_T} \right) U_i. \tag{18}$$
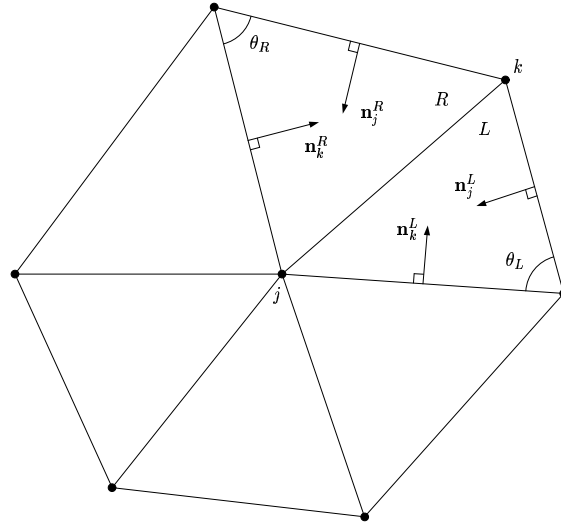
Figure 13. Node-centered stencil on triangular grids. Note that the normals are not scaled.

The first term contains contributions from the node value, U_j, and the second term contains contributions from the neighbors.

We now restrict our attention to two dimensions and specialize (18) to triangular grids (Figure 13):

$$\int_{\Omega_j} \Delta U d\Omega_j = -\frac{1}{4} \sum_{T \in \{\Omega_j\}} \left(\frac{\mathbf{n}_j^T \cdot \mathbf{n}_j^T}{\Omega_T} \right) U_j - \frac{1}{4} \sum_{k \in \{k_j\}} \left(\frac{\mathbf{n}_k^L \cdot \mathbf{n}_j^L}{\Omega_L} + \frac{\mathbf{n}_k^R \cdot \mathbf{n}_j^R}{\Omega_R} \right) U_k, \quad (19)$$

where $\{k_j\}$ is a set of neighbors of j and the normals are scaled inward normals defined as in Figure 13. This can be written also in terms of angles between faces,

$$\int_{\Omega_j} \Delta U d\Omega_j = -\frac{1}{4} \sum_{T \in \{\Omega_j\}} \left(\frac{\mathbf{n}_j^T \cdot \mathbf{n}_j^T}{\Omega_T} \right) U_j + \frac{1}{2} \sum_{k \in \{k_j\}} \left(\cot \theta_L + \cot \theta_R \right) U_k, \quad (20)$$

and is often used to show that the discretization is positive for triangulations with $\theta_L + \theta_R < \pi$. Consider now a triangular grid shown in Figure 14, which is constructed by inserting diagonals into a Cartesian grid. For this particular diagonal splitting, the node 3 does not contribute to the discretization (20) because this node is not a neighbor to the node j, and also the nodes 1, 5, and 7 do not contribute because the angles θ_L and θ_R are both $90°$ and therefore the coefficient $(\cot \theta_L + \cot \theta_R)$ vanishes. This is, in fact, true for *any diagonal splittings*: contributions from the corner nodes, 1, 3, 5, 7, are always zero either because it is not in the actual stencil or because the coefficient vanishes. Observe also that the angles θ_L and θ_R for other nodes are independent of the
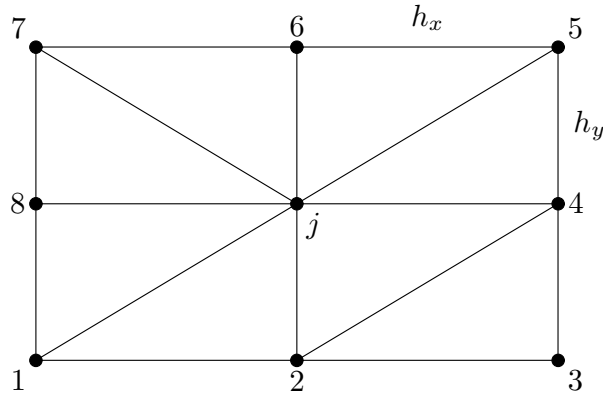
Figure 14. Triangular grid with arbitrary aspect ratio.

diagonal splitting, and thus we always have

$$
\cot \theta_L = \cot \theta_R =
\begin{cases}
\dfrac{h_y}{h_x} & \text{for nodes } 2 \text{ and } 6, \\[2ex]
\dfrac{h_x}{h_y} & \text{for nodes } 4 \text{ and } 8.
\end{cases}
\tag{21}
$$

Moreover, it is easy to show that the coefficient of U_j is also independent of the splitting. Hence, the discretization (20) can be written, for arbitrary splittings, as

$$
\int_{\Omega_j} \Delta U \, d\Omega_j = -2 \left(\frac{h_x}{h_y} + \frac{h_y}{h_x} \right) U_j + \frac{h_y}{h_x} U_2 + \frac{h_x}{h_y} U_4 + \frac{h_y}{h_x} U_6 + \frac{h_x}{h_y} U_8
\tag{22}
$$

$$
= h_x h_y \left(\frac{U_4 - 2U_j + U_8}{h_x^2} + \frac{U_6 - 2U_j + U_2}{h_y^2} \right).
\tag{23}
$$

This is nothing but a common finite-difference discretization. Therefore, the node-centered (Galerkin) discretization of the Laplacian is equivalent to a common finite-difference discretization for triangular grids for rectangular geometries with arbitrary diagonal splitting and aspect ratio. For stretched grids where h_x varies in x-direction and/or h_y varies in y-direction, the corner nodes still do not contribute to the discretization.

In three dimensions, the node-centered discretization does not generally reduce to a common finite-difference discretization even for a regular tetrahedral grid which can be constructed from a Cartesian grid by dissecting each cube into five or six tetrahedra. It can become equivalent precisely to the standard finite-difference discretization in a very special case where a node is originally centered at a common 7-point finite-difference stencil. In general, a solution at a node will be coupled with almost all solutions at the edge-adjacent neighbor nodes because the dot

product $(\mathbf{n}_i \cdot \mathbf{n}_j^T)$ in (18) rarely vanishes. However, actual coefficients for neighbor solutions are generally much larger at nodes in a common finite-difference stencil than at other nodes.

References

[1]Thomas, J. L., Diskin, B., and Rumsey, C. L., "Towards Verification of Unstructured-Grid Solvers," *AIAA Journal*, Vol. 46, No. 12, December 2008, pp. 3070–3079.

[2]Holmes, D. G. and Connell, S. D., "Solution of the 2D Navier-Stokes equations on unstructured adaptive grids," AIAA Paper 89-1392, 9-th AIAA CFD conference, Washington, DC, June 1989.

[3]Rausch, R. D., Batina, J. T., and Yang, H. T., "Spatial adaptation procedures on unstructured meshes for accurate unsteady aerodynamic flow computation," AIAA Paper 89-1392, 9-th AIAA CFD conference, Washington, DC, June 1989.

[4]Frink, N. T., "Assesment of an unstructured-grid method for predicting 3-D turbulent viscous flows," AIAA Paper 96-0292, 34-nd AIAA Aerospace Science Meeting and Exhibit, Reno, NV, January 1996.

[5]Haselbacher, A. C., "On constrained reconstruction operators," AIAA Paper 2006-1274, 44-th AIAA Aerospace Science Meeting and Exhibit, Reno, NV, January 2006.

[6]Barth, T. J., "Numerical Aspects of Computing High-Reynolds Number Flow on Unstructured Meshes," AIAA Paper 91-0721, 29-th AIAA Aerospace Science Meeting, Reno, NV, January 1991.

[7]Coirier, W. J., "An Adaptively-Refined, Cartesian, Cell-Based Scheme for the Euler and Navier-Stokes Equations," Tech. rep., NASA TM-106754, October 1994.

[8]Frink, N. T., "Tetrahedral Unstructured Navier-Stokes Methods for Turbulent Flows," *AIAA Journal*, Vol. 36, No. 11, 1998, pp. 1975–1982.

[9]Mavriplis, D. J., "Revisiting the Least-Square Procedure for Gradient Reconstruction on unstructured Meshes," AIAA Paper 2003-3986, 18-th AIAA CFD conference, Orlando, FL, June 2003.

[10]Petrovskaya, N. V., "The choice of weight coefficients for least-square gradient approximation," *J. Math. Mod.*, Vol. 16(5), 2004, pp. 83–93, (in Russian).

[11]Smith, T. M., Barone, M. F., Bond, R. B., Lorber, A. A., and Baur, D. G., "Comparison of Reconstruction Techniques for Unstructured Mesh Vertex Centered Finite Volume Scheme," Tech. rep., 18-th AIAA CFD Conference, Miami, FL, June 2007, AIAA Paper 2007-3958.

[12]Anderson, W. K. and Bonhaus, D. L., "An implicit upwind algorithm for computing turbulent flows on unstructured grids," *Computers and Fluids*, Vol. 23, No. 1, 1994, pp. 1–21.

[13]Haselbacher, A. C., *A Grid-Tranparent Numerical Method for Compressible Viscous Flow on Mixed Unstructured Meshes*, Ph.D. thesis, Loughborough University, 1999.

[14]Haselbacher, A. C., McGuirk, J. J., and Page, G. J., "Finite-Volume Discretization Aspects for Viscous Flows on Mixed Unstructured Grids," *AIAA Journal*, Vol. 37, 1999, pp. 177–184.

[15]Diskin, B. and Thomas, J. L., "Accuracy Analysis for Mixed-Element Finite-Volume Discretization Schemes," Tech. rep., NIA Report 2007-08, National Institute of Aerospace, August 2007.

[16]Diskin, B., Thomas, J. L., Nielsen, E. J., Nishikawa, H., and White, J. A., "Comparison of Node-Centered and Cell-Centered Unstructured Finite-Volume Discretizations. Part I: Viscous Fluxes," AIAA Paper 2009-597, 47-th AIAA Aerospace Sciencies Meeting, Orlando, FL, January 2009.

[17] Hirsch, C., *Numerical computation of internal and external flows. Vol.1, Fundumentals of numerical discretization*, A Wiley-Interscience publication, John Wiley & Sons, Inc., 605 Third Avenue, New York, NY 10158-0012, USA, 1988.

[18] Syrakos, A. and Goulas, A., "Estimate of the Truncation Error of Finite Volume Discretization of the Navier-Stokes Equations on Collocated Grids," *Int. J. Numer. Meth. Fluids*, Vol. 50, 2006, pp. 103–130.

[19] Turkel, E., "Accuracy of Schemes with Nonuniform Meshes for Compressible Fluid Flows," *Applied Numerical Mathematics*, Vol. 2, 1986, pp. 529–550.

[20] Giles, M. B., "Accuracy of node-based solutions on irregular meshes," *11-th International Conference on Numerical Methods in Fluid Dynamics*, edited by D. L. Dwoyer, M. Y. Hussaini, and R. Voigt, Lecture Notes in Physics, v. 323, Springer-Verlag, 1989, pp. 369–373.

[21] Lindquist, D. R. and Giles, M. B., "A comparison of numerical schemes on triangular and quadrilateral meshes," *11-th International Conference on Numerical Methods in Fluid Dynamics*, edited by D. L. Dwoyer, M. Y. Hussaini, and R. Voigt, Lecture Notes in Physics, v. 323, Springer-Verlag, 1989, pp. 273–277.

[22] Manteuffel, T. A. and White, A. B., "The numerical solution of the second-order boundary value problem on nonuniform meshes," *Mathematics of Computations*, Vol. 47(176), October 1986, pp. 511–536.

[23] Diskin, B. and Thomas, J. L., "Accuracy of Gradient Reconstruction on Grids with High Aspect Ratio," Tech. rep., NIA Report 2008-12, National Institute of Aerospace, December 2008.